

Article

A Sustainable Steel-GFRP Composite Bars Reinforced Concrete Structure: Investigation of the Bonding Performance

Guoliang Huang¹, Ji Shi¹, Wenzhuo Lian¹, Linbo Hong², Shuzhuo Zhi², Jialing Yang^{2,3}, Caiyan Lin¹, Junhong Zhou¹ and Shuhua Xiao^{2,4,*}

¹ Huizhou Power Supply Bureau, Guangdong Power Grid Co., Ltd., China Southern Power Grid Co., Ltd., Huizhou 516000, China

² School of Civil and Transportation Engineering, Guangdong University of Technology, Guangzhou 510006, China

³ School of Civil Engineering, Central South University, Changsha 410083, China

⁴ Department of Civil Engineering, Dongguan University of Technology, Dongguan 523080, China

* Correspondence: xiaoshuhua@dgut.edu.cn

Abstract: Steel-fiber reinforced polymer (FRP) composite bars (SFCBs) can enhance the controllability of damage in concrete structures; thus, studying the interfacial bonding between them is fundamental and a prerequisite for achieving deformation coordination and collaboration. However, research on the interfacial bonding performance between SFCBs and concrete remains inadequate. This study conducted central pullout tests on SFCB-concrete specimens with different concrete strengths (C30, C50, and C70), bar diameters (12, 16 and 20 mm), and hoop reinforcement constraints, analyzing variations in failure modes, bond-slip curves, bond strength, etc. Additionally, finite element simulations were performed using ABAQUS software to further validate the bonding mechanism of SFCB-concrete. The results showed that the failure mode of the specimens was related to the confinement effect on the bars. Insufficient concrete cover and lack of hoop restraint led to splitting failure, whereas pullout failure occurred otherwise. For the specimens with pullout failure, the interfacial damage between the SFCB and concrete was mainly caused by the surface fibers wear of the bar and the shear of the concrete lugs, which indicated that the bond of the SFCB-concrete interface consisted mainly of mechanical interlocking forces. In addition, the variation of concrete strength as well as bar diameter did not affect the bond-slip relationship of SFCB-concrete. However, the bond strength of SFCB-concrete increased with the increase of concrete strength. For example, compared with C30 concrete, when the concrete strength was increased to C70, the bond strength of the specimens under the same conditions was increased to 50–101.6%. In contrast, the bond strength of the specimens decreased by 13.29–28.71% when the bar diameter was increased from 12 to 14 mm. These discoveries serve as valuable references for the implementation of sustainable SFCB-reinforced concrete structures.

Keywords: bond-slip; fiber reinforced polymer (FRP); steel-FRP composited bars (SFCBs); bond strength



Citation: Huang, G.; Shi, J.; Lian, W.; Hong, L.; Zhi, S.; Yang, J.; Lin, C.; Zhou, J.; Xiao, S. A Sustainable Steel-GFRP Composite Bars Reinforced Concrete Structure: Investigation of the Bonding Performance. *Buildings* **2024**, *14*, 1249. <https://doi.org/10.3390/buildings14051249>

Academic Editors: Xiaoyong Wang and Mohamed K. Ismail

Received: 25 March 2024

Revised: 23 April 2024

Accepted: 26 April 2024

Published: 28 April 2024



Copyright: © 2024 by the authors. Licensee MDPI, Basel, Switzerland. This article is an open access article distributed under the terms and conditions of the Creative Commons Attribution (CC BY) license (<https://creativecommons.org/licenses/by/4.0/>).

1. Introduction

With the construction and development of marine engineering, the issue of structural durability caused by steel corrosion is receiving increasing attention [1,2]. Using fiber-reinforced polymer (FRP) bars with excellent corrosion resistance, which are lightweight and high strength, produced through pultrusion technology, as an alternative to steel reinforcement in marine concrete structures is one of the most popular approaches to addressing durability issues [3–5]. However, the poor ductility and low elastic modulus of the FRP limits its direct application in structures [6]. Therefore, a new type of reinforcement material called Steel-FRP composite bars (SFCBs) [7] has emerged, which wraps FRP around a steel core [8]. Although existing studies indicate that water molecules diffuse within the FRP in the direction of the resin and fiber-resin interface in marine environments, thereby

degrading the performance of the FRP [9,10], in general, FRP still exhibits better seawater corrosion resistance compared to steel reinforcement. Cai et al. [11] demonstrated that the degradation mechanism of SFCBs under seawater immersion is the degradation of the FRP layer without corrosion of the inner steel. The study by Zhou et al. [12] suggests that the corrosion resistance of SFCBs is 10 times better (for carbon fiber type) or even 100 times better (for glass fiber type) than that of conventional steel bars. This indicates that the FRP layer can effectively isolate corrosive substances such as seawater from the inner steel, enabling SFCBs to combine the ductility of steel bars with the corrosion resistance of FRP. This can extend the lifespan of reinforced concrete structures in marine environments, showing promising prospects [8,11,13,14].

SFCBs exhibit a double-sigmoid stress-strain relationship under uniaxial tension [11,14]. The outer layer of FRP functions dually as a protective barrier against corrosion for the inner core steel bars, while concurrently sharing the tensile loads with them [11]. The exceptional tensile strength and linear elastic properties of FRP enable it to sustain tensile loads even after the inner core steel bars yield, thereby providing SFCBs with a reliable post-yield modulus. In contrast to FRP bars, SFCBs exhibit a superior elastic modulus and a distinct yield point, attributed to the integration of the steel bars. Consequently, concrete members reinforced with SFCBs possess remarkable durability [15]. Furthermore, when compared to concrete members reinforced with FRP bars, SFCB-reinforced concrete members demonstrate reduced deflections and crack widths under bending moments [16]. Notably, compared to traditional reinforced concrete members, SFCB-reinforced concrete members exhibit remarkable secondary stiffness post-yield, a high safety margin in load-bearing capacity, and superior deformation recovery after earthquakes [17].

The bond between the reinforcing bars and concrete interface serves as the fundamental prerequisite for coordinated deformation and resistance to external forces [18–21]. While direct studies on the interfacial properties of the FRP layer and the steel reinforcement are lacking, numerous studies have shown that the stress-strain behavior of SFCBs under tension follows the mixture law [8,11,14,20]. This implies that the stress-strain relationship of SFCBs can be determined by combining the stiffness equivalence method based on parameters such as the elastic modulus and cross-sectional area of the FRP and inner steel. This indirectly suggests a good bond between the FRP layer and the inner steel, ensuring their effective collaboration. Therefore, this study does not consider the influence of interfacial slip between the FRP layer and the inner core reinforcement on the SFCB-concrete bond performance.

Understanding the bond-slip behavior is of utmost importance for subsequent theoretical research and engineering design [22,23]. SFCBs exhibit unique yield points and strain hardening characteristics under uniaxial tension, adhering to a double-sigmoid stress-strain model [8,14], exhibiting mechanical properties distinct from those of FRP bars and steel reinforcement. Zhao et al. [24] conducted a study examining the adhesive strength between concrete and SFCB, considering various processing techniques and surface treatments, revealing that the adhesive strength of SFCBs lies between plain steel and deformed steel. Xu et al. [25] investigated the influence of various SFCB diameters, matrix types, compressive strength of engineered cementitious composites (ECC), and reinforcement types on the bond strength of the SFCB-ECC interface, demonstrating that ECC specimens exhibit higher bond strength compared to concrete specimens with equivalent compressive strength. Dong et al. [26,27] investigated the impact of various aging durations and environments on the interfacial bonding performance between SFCBs and seawater-sea sand concrete. Ge et al. [28] analyzed the impact of FRP type, sustained stress level, chloride concentration, and aging time on the adhesive strength of the SFCB-concrete interface, establishing a bond-slip model specific to SFCB-concrete. While these studies have provided partial insights into the interfacial bond properties of SFCB-concrete, there remains a paucity of research on the influence of ordinary concrete strength, hoop reinforcement confinement, and thickness of the GFRP layer (bar diameter) on the bond properties of the

SFCB-concrete interface. Given its significance for the application of SFCBs in structures, further in-depth research in this area is imperative.

For the above-mentioned discussion, central pullout tests were conducted on the SFCB-concrete interface to study the effect of bar diameter, hoop reinforcement confinement, and concrete strength regarding SFCB-concrete bond-slip. A bond-slip relationship model suitable for ribbed SFCB-concrete interfaces was proposed based on existing models. Additionally, finite element analysis was performed using ABAQUS 2016 to establish a finite element model of the SFCB-concrete central pullout test, validating the impact of the research parameters influencing the bond-slip behavior. This study offers valuable insights for future research and applications involving SFCBs.

2. Pullout Test

2.1. Material

The three types of SFCBs employed in this study are illustrated in Figure 1, designated as GS12, GS16, and GS20, with respective outer fiber thicknesses of 2, 4, and 6 mm. The inner core of each SFCB comprises an HPB400-grade plain round 8 mm-diameter steel bar. The yield strength of the inner steel core is 468 MPa, with an elastic modulus of 185 GPa. The outer GFRP layer has an elastic modulus of 49.8 GPa and a tensile strength of 854.6 MPa. The SFCBs utilized in this study, supplied by Jiangsu Haichuan New Materials Technology Co., Ltd., Jurong, China, were fabricated by uniformly arranging glass fiber bundles impregnated with resin along the surface of the steel bar. Subsequently, pultrusion molding technology was employed for fabrication, utilizing equipment similar to that used for manufacturing FRP reinforcement, thereby minimizing additional production costs. The SFCBs feature helical ribs formed by winding nylon threads around the bar surface. These ribs have a height of approximately 1 mm and a spacing of around 10 mm. The bars' composition includes a 64% volume fraction of GFRP glass fibers embedded in a matrix of unsaturated polyester resin, type 5562 A-N-1. In accordance with the Chinese standard GB/T 30022-2013 [29], tensile tests were carried out on the bars, with five replicate specimens in each group, and the results are shown in Table 1. Figure 2 shows the stress-strain relationship curves for one of the specimens of the three SFCBs.

As depicted in Figure 2, the relationship between stress and strain for SFCBs exhibits a bilinear pattern. Wu et al. [8] proposed the constitutive model of SFCBs under uniaxial tension based on composite material theory, as shown in Equations (1) and (2),

$$\sigma = \begin{cases} E_I \varepsilon & 0 \leq \varepsilon \leq \varepsilon_y \\ E_I \varepsilon_y + E_{II} (\varepsilon - \varepsilon_y) & \varepsilon_y \leq \varepsilon \leq \varepsilon_u \end{cases} \quad (1)$$

$$E_I = \frac{E_s A_s + E_f A_f}{A}, \quad E_{II} = \frac{E_f A_f}{A} \quad (2)$$

where σ is the stress within the cross-section of the SFCB, while E_I and E_{II} denote the elastic modulus and post-yield modulus of the composite reinforcement, respectively. ε is the tensile strain of SFCB, ε_y and ε_u are the yield strain and ultimate strain of SFCB under uniaxial tension, respectively, which can be determined from the tensile strength and elastic modulus of the steel and FRP bars provided earlier. E_s and A_s are the elastic modulus and cross-sectional area of the inner core steel reinforcement. E_f and A_f are the elastic modulus and cross-sectional area of the outer GFRP layer, and A is the cross-sectional area of SFCB. By calculating the mechanical parameters of SFCBs according to Equations (1) and (2), as shown in Table 1, the calculated values align well with the laboratory results. Consequently, the bilinear model can be utilized to simulate the tensile stress-strain relationship of SFCBs in this experiment. It is important to note that despite the excellent post-yield tensile performance of SFCBs, to ensure adequate stiffness of the structure throughout its service life, the design tensile strength of SFCBs applied in engineering should not exceed their yield strength. In other words, the stress-strain relationship of the first stage of SFCBs should be utilized in engineering design.



Figure 1. SFCBs.

Table 1. Material performance parameters of bars.

| Bars | E_I (GPa) | | | | E_{II} (Gpa) | | | | f_y (Mpa) | | | | f_u (Mpa) | | | |
|------|-------------|------|-------|-----------|----------------|------|------|-----------|-------------|------|-------|-----------|-------------|------|-------|-----------|
| | T | SD | C | Error (%) | T | SD | C | Error (%) | T | SD | C | Error (%) | T | SD | C | Error (%) |
| GS12 | 113.1 | 0.94 | 109.8 | 3.0 | 31.2 | 1.26 | 28.5 | 9.6 | 267.6 | 2.06 | 263.5 | 1.5 | 600.4 | 8.13 | 658.7 | −8.8 |
| GS16 | 80.7 | 0.56 | 84.2 | −4.2 | 31.4 | 1.70 | 38.5 | −18.5 | 191.1 | 2.68 | 214.2 | −10.8 | 428.7 | 8.60 | 729.1 | −41.2 |
| GS20 | 69.5 | 1.36 | 72.3 | −3.9 | 43.0 | 0.92 | 48.3 | −12.4 | 176.1 | 4.71 | 173.5 | 1.5 | 542.0 | 9.25 | 761.7 | −28.8 |

Note: f_y is the yield strength, and f_u is the ultimate strength, T is the average test value, C is the calculated value, SD is the standard deviation of test value.

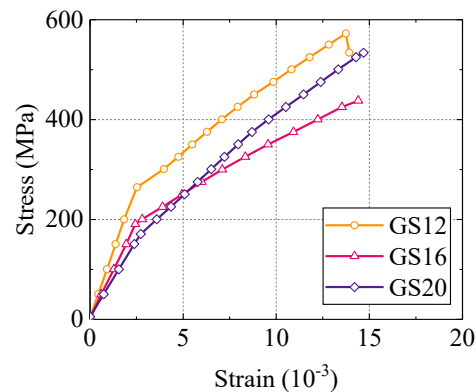


Figure 2. Stress-strain curve of SFCBs.

To investigate the influence of concrete strength, experiments were conducted using three strength grades of concrete: C30, C50, and C70. The mix proportions of concrete are shown in Table 2. The experiment used 42.5R grade Portland cement, with medium-grade river sand as fine aggregate and crushed stones with a particle size range of 5–20 mm as coarse aggregate. Both coarse and fine aggregates were sieved, washed, and dried before use. Mechanical performance tests were carried out on cubic specimens with a side length of 150 mm and cylindrical specimens with dimensions of $\Phi 150 \times 300$ mm according to the Chinese standard GB50081-2019 [30], and the results are summarized in Table 2.

Table 2. Detailed parameters of concrete.

| Specimen | Cement /(kg/m ³) | Sand /(kg/m ³) | Coarse Aggregate /(kg/m ³) | Water /(kg/m ³) | Sand Rate/% | WRA/(kg/m ³) | f_{cu} /MPa | f_c /MPa | E_c /GPa | ν |
|----------|---------------------------------|-------------------------------|----------------------------------------------|--------------------------------|----------------|--------------------------|------------------|---------------|---------------|-------|
| C30 | 396.55 | 698.74 | 1074.7 | 230 | 39.4 | / | 41.42 | 37.95 | 26.66 | 0.2 |
| C50 | 469.39 | 598.62 | 1102.0 | 230 | 35.2 | / | 60.57 | 53.34 | 29.33 | 0.2 |
| C70 | 477.40 | 560.10 | 1190.2 | 172 | 32.0 | 5 | 78.82 | 72.16 | 34.15 | 0.2 |

Note: f_{cu} is the cubic compressive strength of concrete, f_c is the cylindrical compressive strength of concrete, E_c is the elastic modulus of concrete, and ν is the Poisson's ratio of concrete.

2.2. Specimen Design

The design diagram of the pullout test specimens is illustrated in Figure 3. Drawing reference from the standard GB/T 30022-2013 [29], 30 centrally-located pullout specimens were fabricated and prepared to explore the influence of reinforcement diameter, concrete strength, and stirrup confinement on the adhesive performance between SFCB and concrete. As shown in Figure 3, the concrete component is represented by a cubic block with a side length of 200 mm. Additionally, considering the limitations of the testing equipment used in this study, the total length of the specimens was determined to be 600 mm. The bonding region is situated at the center of the concrete block, with a bond length, designated as l_b , five times the diameter, d_b , of the reinforcement. PVC tubing is employed in the non-bonding region to isolate the reinforcement from the concrete. To maintain a constant bond length during the pullout test, a 50 mm length of reinforcement is left exposed at the free end of each specimen. For specimens incorporating stirrup confinement, two stirrups of 8 mm diameter and HPB300 grade are inserted within the bonding zone.

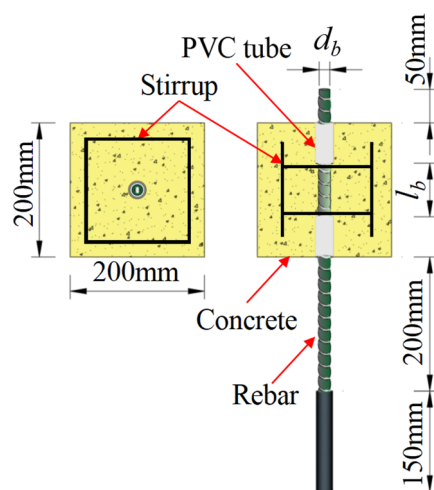


Figure 3. Specimen design.

2.3. Test Setup

The experimental arrangement is depicted in Figure 4, where the pullout test is conducted on the MTS-250 kN material testing system. Two displacement sensors are placed at the fixed end of the specimen to monitor the displacement of the reinforcement material. Following the specifications outlined in GB/T 30022-2013 [29], the loading protocol employs a displacement control mode with a loading rate of 1 mm/min. The test is terminated when the rebar is pulled out, split, or fractured.

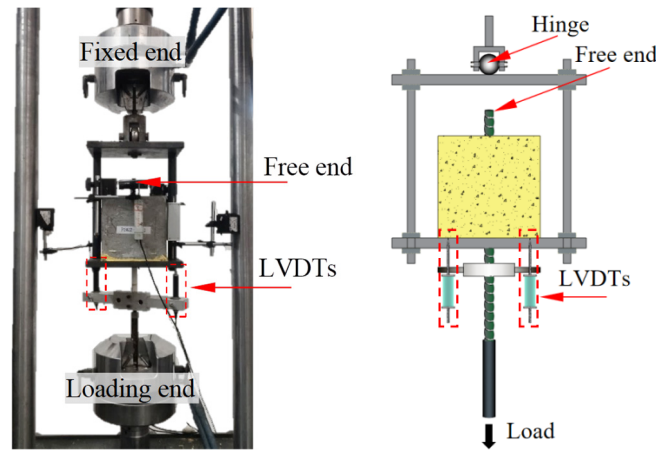


Figure 4. Test setup.

3. Results and Discussion

The bond stress at the SFCB-concrete interface is represented by the average interface shear stress [22], as shown in Equation (3). In the equation, τ and P represent to the bond stress and tensile load, respectively, exhibited by the SFCBs during the pullout operation.

$$\tau = \frac{P}{\pi d_b l_b} \tag{3}$$

The curve of bond versus slip and corresponding results of the SFCB-concrete interface can be obtained based on Equation (3), as shown in Figure 5 and Table 3.

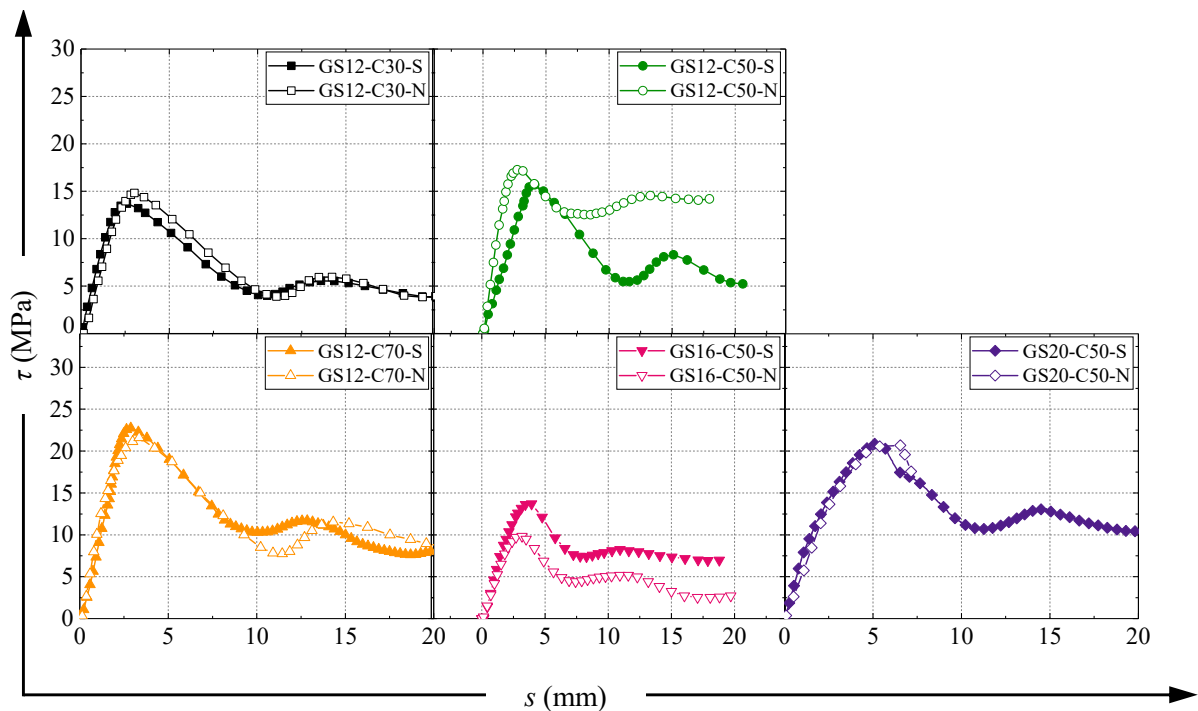


Figure 5. Bond-Slip curve of the SFCB-concrete interface.

Table 3. Summary of FSCBs drawing test results.

| Specimens | P_u (kN) | P_u^a (kN) | τ_1 (MPa) | τ_1^a (MPa) | s_1 (mm) | s_1^a (mm) | Failure Mode |
|--------------|---------------|-----------------|-------------------|---------------------|---------------|-----------------|--------------|
| GS12-C30-N-1 | 33.5 | | 14.8 | | 3.3 | | P |
| GS12-C30-N-2 | 28.1 | 33.0 | 12.4 | 14.6 | 2.7 | 3.3 | P |
| GS12-C30-N-3 | 37.3 | | 16.5 | | 3.9 | | P |
| GS12-C30-S-1 | 31.4 | | 13.9 | | 3.1 | | P |
| GS12-C30-S-2 | 21.6 | 28.0 | 9.6 | 12.4 | 3.5 | 3.1 | P |
| GS12-C30-S-3 | 30.9 | | 13.7 | | 2.6 | | P |
| GS12-C50-N-1 | 21.3 | | 9.5 | | 2.6 | | P |
| GS12-C50-N-2 | 42.1 | 33.0 | 18.8 | 14.7 | 3.2 | 3.3 | P |
| GS12-C50-N-3 | 35.5 | | 15.7 | | 4.0 | | P |
| GS12-C50-S-1 | 29.4 | | 13.0 | | 3.2 | | P |
| GS12-C50-S-2 | 39.0 | 35.6 | 17.3 | 15.8 | 3.5 | 3.5 | P |
| GS12-C50-S-3 | 38.5 | | 17.1 | | 3.9 | | P |
| GS12-C70-N-1 | 48.7 | | 21.9 | | 3.8 | | P |
| GS12-C70-N-2 | / | 48.7 | / | 21.9 | / | 3.8 | F |
| GS12-C70-N-3 | / | | / | | / | | F |
| GS12-C70-S-1 | 51.3 | | 22.7 | | 2.5 | | P |
| GS12-C70-S-2 | 57.8 | 56.6 | 25.3 | 25.0 | 2.7 | 2.8 | P |
| GS12-C70-S-3 | 60.8 | | 26.9 | | 3.3 | | P |
| GS16-C50-N-1 | 39.6 | | 9.5 | | 3.4 | | P |
| GS16-C50-N-2 | 41.1 | 50.2 | 10.2 | 12.3 | 3.3 | 4.7 | P |
| GS16-C50-N-3 | 70.0 | | 17.3 | | 7.3 | | P |
| GS16-C50-S-1 | / | | / | | / | | F |
| GS16-C50-S-2 | 55.2 | 55.2 | 13.7 | 13.7 | 3.5 | 3.5 | P |
| GS16-C50-S-3 | / | | / | | / | | F |
| GS20-C50-N-1 | 89.8 | | 14.0 | | 6.0 | | S |
| GS20-C50-N-2 | 131.7 | 117.7 | 21.0 | 18.7 | 6.2 | 6.1 | S |
| GS20-C50-N-3 | 131.7 | | 21.0 | | 6.1 | | S |
| GS20-C50-S-1 | 124.9 | | 19.9 | | 5.0 | | P |
| GS20-C50-S-2 | 131.1 | 132.7 | 20.9 | 21.0 | 5.3 | 5.2 | P |
| GS20-C50-S-3 | 142.1 | | 22.2 | | 5.4 | | P |

Note: The first item of the specimen number represents the type of reinforcement used; the second item represents the concrete grade; the third item indicates N for specimens without stirrups and S for specimens with stirrups; the fourth item is the repeat specimen number; P_u is the maximum pullout force; τ_1 and s_1 represent the bond strength and the corresponding peak slip, respectively; the superscript 'a' denotes the average value of the reorganized test results; for failure modes, P represents pullout failure, and S represents splitting failure.

3.1. Failure Mode

The typical interface failure modes in pullout tests, as shown in Figure 6, include pullout failure and splitting failure. The majority of specimens experienced pullout failure. Notably, the GS20-C50-N specimen experienced splitting failure due to insufficient lateral restraint provided by the concrete cover layer resulting from the larger diameter of the reinforcement. In contrast, the GS20-C50-S specimen with the same diameter exhibited pullout failure as the concrete cracks did not propagate to form splitting cracks under the effective confinement of the stirrups. Additionally, some specimens experienced reinforcement fracture, which is not considered an interface failure mode and will therefore not be further analyzed.



Figure 6. Failure mode.

To observe the failure morphology at the interface between the SFCB and concrete, specimens without stirrups were symmetrically split along the neutral axis. The resulting typical interface failure morphology between the reinforcement and concrete is shown in Figure 7. In this figure, the upper end represents the side near the free end, while the lower end corresponds to the side nearer the loading end. From Figure 7, it can be clearly seen that specimens experiencing pullout failure exhibit an interface damage mechanism that involves surface fiber wear or shear failure of the concrete between ribs. This damage is attributed to the mechanical interlock mechanism at the interface, indicating that the bond strength of ribbed bars is primarily governed by mechanical interlocking forces. On the other hand, specimens which experienced splitting failure, such as GS20-C50-N, are regulated by the radial tensile strength of the concrete. Consequently, no significant mechanical interlock damage was observed at the SFCB-concrete interface in these cases. Based on the above analysis, it can be concluded that the interfacial bonding mechanism of SFCB-concrete is similar to that described in the literature [31,32] for FRP-concrete.

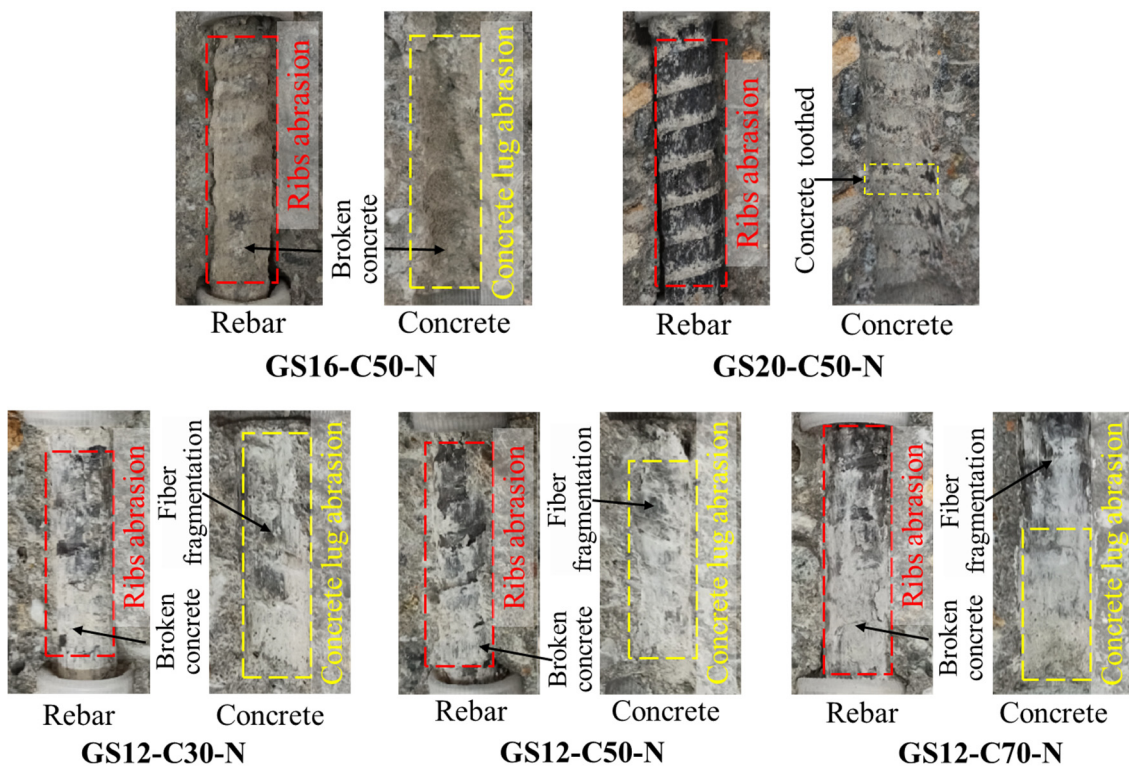


Figure 7. Interfacial damage condition.

3.2. Bond Slip Curve

As depicted in Figure 5, the shape of the bond-slip curve for SFCB-concrete can primarily be categorized into three distinct stages, where the bond strength is composed of chemical adhesion, friction, and mechanical interlocking forces [22,23]. The first stage is the ascending stage, where the chemical adhesion ceases to work upon the occurrence of slip, and the controlling factor of bond strength gradually transitions from primarily friction and chemical adhesion to predominantly mechanical interlocking, as shown in Figure 8a. As the amount of slip increases, the concrete positioned between the ribs is gradually cracked due to the mechanical interlocking forces, resulting in wear on the rib surfaces of the reinforcement and a gradual increase in bond stress until it reaches a peak. During this process, the radial component of the mechanical interlocking forces is balanced by the radial force provided by the concrete cover or stirrups. When radial restraint is insufficient, radial cracks in the concrete propagate to the surface of the specimen, leading to splitting failure, and subsequently, a rapid loss of bond strength. Conversely, when radial restraint is sufficient, the radial crack development in the concrete is limited, and the bond strength is controlled by the shear strength of the concrete between the ribs and the reinforcement. When shear failure occurs in the concrete between the ribs, the mechanical interlocking force at the interface gradually diminishes, and the bond-slip curve enters the second stage, as shown in Figure 8b. The second stage is the descending stage, where the bond strength is primarily controlled by friction due to the gradual failure of mechanical interlocking. As shown in Figure 8c, the residual stage exhibits a wavy pattern in the bond-slip curve. This is because the surface shear stiffness of the SFCBs is relatively low, and during the pullout process, shear wear occurs on the ribs, resulting in partial preservation of the concrete between the ribs. When subsequent ribs engage with the concrete, some mechanical interlocking forces are still generated, leading to a wavy variation in bond stress.

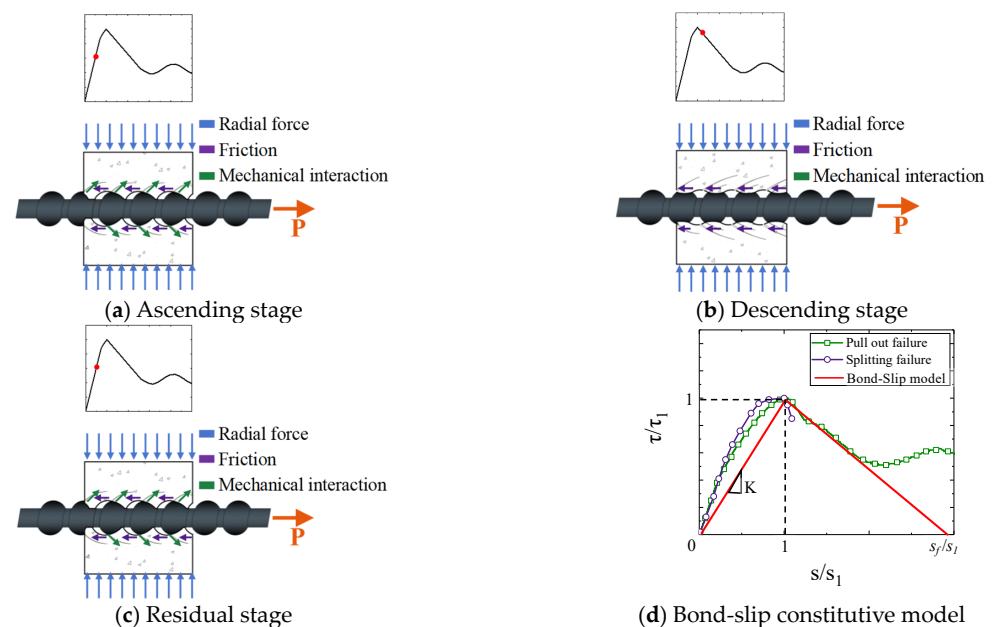


Figure 8. SFCB-concrete interface bond-slip relationship.

Based on the preceding analysis, it becomes evident that the bond stress-slip relationship between the SFCB and concrete is primarily governed by the mechanical interlocking between the ribs and concrete. To facilitate subsequent finite element analysis, the present study employs the bilinear bond-slip model depicted in Figure 8d to replicate the bond-slip behavior of SFCB-concrete, as expressed in Equations (4)–(6). In these equations,

τ_1 signifies the peak bond strength, with s_1 representing its corresponding slip value, whereas s_f designates the ultimate slip value.

$$\tau = \begin{cases} \tau_1 \frac{s}{s_1}, & s \leq s_1 \\ \tau_1 \frac{s_f - s}{s_f - s_1}, & s_1 < s \leq s_f \\ 0, & s > s_f \end{cases} \quad (4)$$

$$s_f = 2G_f / \tau_1 \quad (5)$$

$$G_f = \frac{1}{2} \tau_1 s_f \quad (6)$$

3.3. Parameter Impact Analysis

3.3.1. Concrete Strength

Figure 9 demonstrates the variation in bonding performance under different concrete strengths. As Figure 9a illustrates, SFCB-concrete exhibits similar bond-slip relationships across varying concrete strengths. This similarity is attributed to the identical interfacial damage mechanism observed during pullout failure, specifically the shear damage between the GFRP ribs and the concrete. Figure 9b reveals a positive correlation between concrete strength and bond strength τ_1 . The reason for this is that stronger concrete generates a greater mechanical locking force, subsequently enhancing the bond strength. Therefore, concrete strength serves as the primary factor controlling the bond strength at the SFCB-concrete interface, with SFCBs exhibiting a bonding mechanism akin to FRP tendons. Furthermore, Figure 9c indicates that the peak slip corresponding to the bond strength remains relatively constant despite changes in concrete strength. This stability is attributed to the fact that the bonding performance of SFCB-concrete is primarily influenced by the mechanical locking between the ribs and concrete. For specimens experiencing pullout failure, the peak slip is directly proportional to the rib spacing C_R . In this study, the peak slip during pullout failure is approximately $0.35 C_R$.

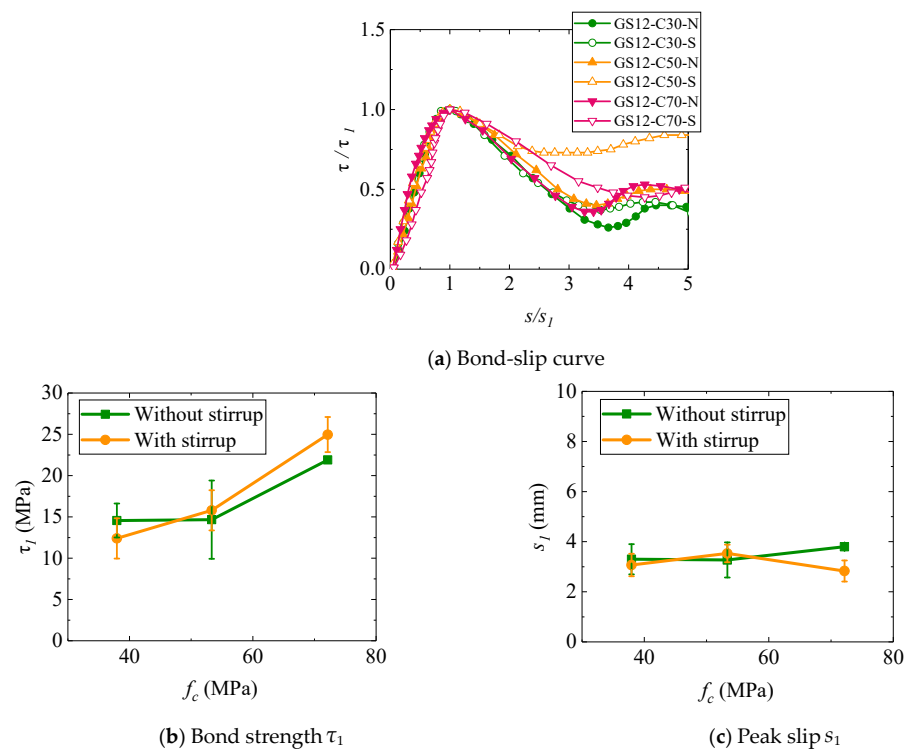


Figure 9. Impact of concrete strength on bonding performance of SFCB-concrete.

3.3.2. Diameter of Reinforcement

Figure 10 presents an investigation into the bonding performance of SFCB-concrete systems with varying tendon diameters. As Figure 10a illustrates, the bond-slip relationships exhibited by the SFCB-concrete interfaces remain similar across different tendon diameters. This similarity is attributed to the consistency in the bonding damage mechanisms observed. Referring to Figure 10b, it can be observed that as the diameter of SFCBs increases from 12 mm to 16 mm, the bond strength decreases by 13.29% (with stirrup) and 28.71% (without stirrup), respectively. These findings align with the conclusions regarding FRP tendon-concrete bonding reported in [23,31,32]. This is due to the fact that in this study, the larger the reinforcement diameter, the smaller the concrete cover, providing less lateral restraint. However, when the diameter of SFCBs increases from 16 mm to 20 mm, the bond strength increases by 48.9% (with stirrup) and 51.38% (without stirrup), respectively. For specimens without stirrups, as the tendon diameter increases, the failure mode at the SFCB-concrete interface changes from pullout failure to splitting failure. This is because the concrete cover provides insufficient radial restraint to large-diameter SFCBs, leading to the radial concrete cracks extending to the surface of the specimen and resulting in splitting failure. As depicted in Figure 10c, the peak slip values for specimens with diameters of 12 mm and 16 mm were comparable, approximately $0.35 C_R$. However, a noteworthy deviation was observed for the 20 mm diameter specimen, as its peak slip value significantly exceeded that of its smaller-diameter counterparts. This discrepancy can be explained by the reduced compressive stress exerted by the SFCBs on the surrounding concrete due to insufficient radial confinement. This delayed the onset of SFCB-concrete interfacial deterioration, facilitating a more uniform distribution of local bond stress from the loaded end to the free end. Consequently, this delay elevated the average bond strength, leading to the observed increase in peak slip.

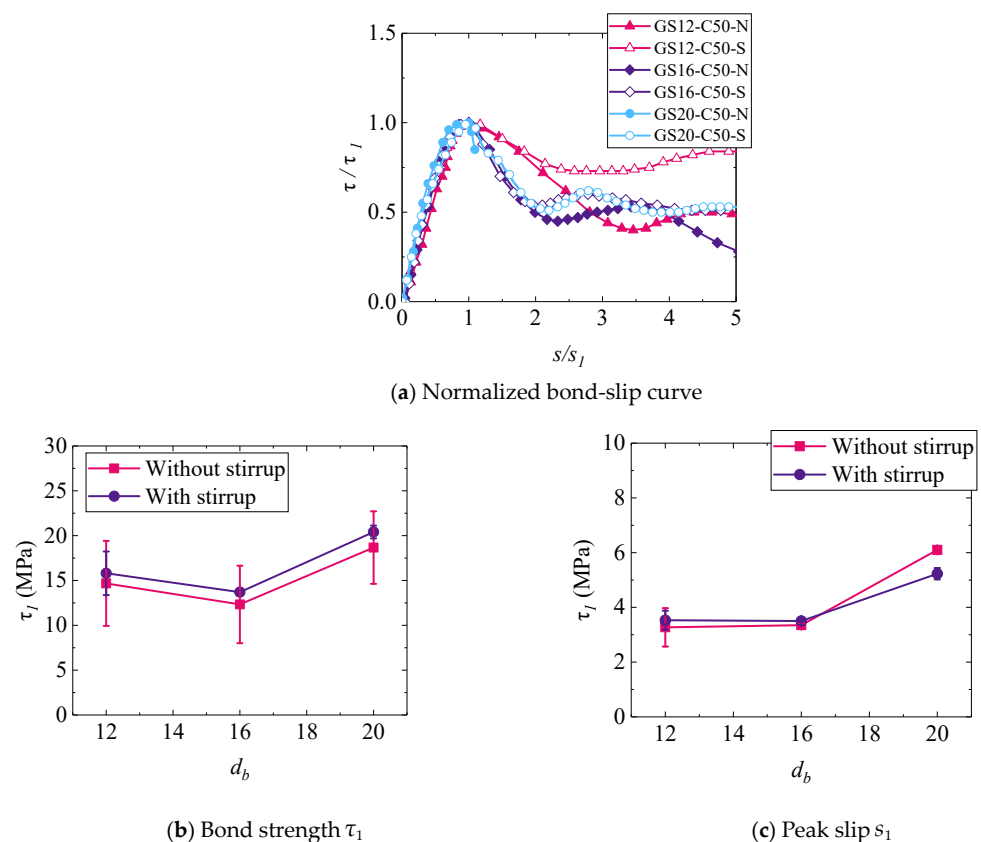


Figure 10. Impact of bars diameter on SFCB-concrete bond performance.

3.3.3. Stirrup Confinement

A comparison between Figures 8 and 10 reveals the influence of stirrup confinement on the bond behavior of SFCB-concrete across varying concrete strengths and reinforcement diameters. Notably, the figures indicate that the inclusion of stirrups has a negligible effect on the interfacial bond performance between the SFCB and concrete. Research by Zhang et al. [33] and Lin et al. [34] indicates that stirrups and concrete cover share a similar mechanism of confinement. There exists a threshold for the confinement provided by either the concrete cover or stirrups to the reinforcement; when the confinement is below this threshold, splitting failure occurs in the specimens. Conversely, when the confinement exceeds this threshold, pullout failure is observed. For specimens without stirrup confinement, this threshold is generally at $c/d_b = 4\sim 5$ [33,34], where c is the thickness of the concrete cover. In this study, the majority of specimens had a c/d_b ratio greater than 5, leading to pullout failure. For the GS20-C50 series of specimens, since $c/d_b = 4.5 < 5$, splitting failure occurred in the absence of stirrup confinement.

3.4. Bond Strength Prediction

In reinforced concrete structures, the stress is transmitted between the reinforcement and the concrete through their bond, making the prediction of the bond strength at the SFCB-concrete interface a crucial issue. ACI 318 [35] and ACI 440.1R [36] provide predictive formulas for the bond strength between steel and FRP reinforcement and concrete, as showed in Equations (7) and (8). These equations account for the influence of concrete cover, bar diameter, and bond length on the bond strength between steel-concrete or FRP-concrete, aligning with the experimental results of SFCB-concrete in this study. While these equations do not consider the effect of transverse reinforcement, given that in this study, the transverse reinforcement mainly affects the failure mode of SFCB-concrete under sufficient lateral confinement, the contribution of transverse reinforcement to bond strength is negligible. Using Equations (7) and (8) to predict the bond strength at the SFCB-concrete interface in this study, the results are illustrated in Figure 11. The standard deviation (STD) and average absolute error (AAE) between the experimental results ($Test_i$) and theoretical predictions ($Theo_i$) were calculated using Equations (9) and (10), where m is the number of specimens.

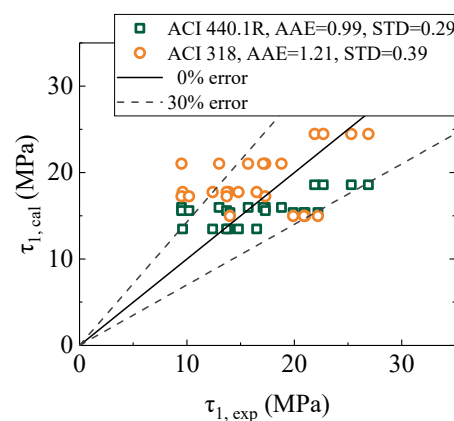


Figure 11. Comparison of Experimental and Predicted bond strength.

From Figure 11, it can be observed that the AAE for bond strength predicted by Equation (7) is 1.21 with a STD of 0.39, whereas for Equation (8), the AAE is 0.99 with an STD of 0.29, indicating that the calculations from Equation (7) tend to overestimate the experimental values, while Equation (8) shows better predictive accuracy. This is attributed to the similar surface properties of SFCB and FRP reinforcement, as well as the similarity in bond failure mechanisms between SFCB-concrete and FRP-concrete. Therefore, it is

recommended to employ the same predictive method as for FRP-concrete to calculate the bond strength at the SFCB-concrete interface, using Equation (8).

$$\tau_1 = 0.083\sqrt{f_c} \left(1.2 + 3\frac{c}{d_b} + 50\frac{d_b}{l_b} \right) \quad (7)$$

$$\tau_1 = 0.083\sqrt{f_c} \left(4 + 0.3\frac{c}{d_b} + 100\frac{d_b}{l_b} \right) \quad (8)$$

$$STD = \sqrt{\frac{\sum_{i=1}^m \left[\frac{Theo_i}{Test_i} - \left(\frac{Theo}{Test} \right)_{aver} \right]^2}{m-1}} \quad (9)$$

$$AAE = \frac{\sum_{i=1}^m \left| \frac{Test_i - Theo_i}{Test_i} \right|}{m} \quad (10)$$

3.5. Design Recommendations

Based on the analysis above, it can be concluded that the effects of concrete strength, bar diameters, and hoop reinforcement on the bond slip behavior of SFCB-concrete are crucial considerations in engineering design. Considering the positive correlation between concrete strength and bond strength, opting for higher strength concrete enhances bond performance, particularly in applications requiring greater load capacity or durability. While larger bar diameters typically result in reduced bond strength, achieving an accurate balance between bond strength and structural requirements is essential. For instance, in cases of unavoidable larger diameters, the use of additional hoop reinforcement can mitigate potential decreases in bond strength and prevent splitting failure. The inclusion of hoop reinforcement should be considered in structural design, especially when dealing with larger diameter rebars or when controlling radial crack formation.

4. Finite Element Analysis

4.1. Model Description

This study utilized finite element software ABAQUS to conduct finite element analysis. Modeling of the pullout specimens is based on the geometric information and loading conditions provided in Figures 3 and 4. The geometric dimensions and mesh discretization of the model are illustrated in Figure 12. For the SFCBs and concrete elements, three-dimensional solid eight-node reduced integration elements (C3D8R) were selected, while stirrups were represented using three-dimensional solid two-node truss elements (T3D2). To establish a confinement relationship between the stirrups and concrete, the embedded region approach was adopted. The outer surface of the concrete features an average mesh size of 4 mm. To precisely capture the dynamics at the reinforcement-concrete junction, the mesh size along the contact surface was narrowed down to 2 mm.

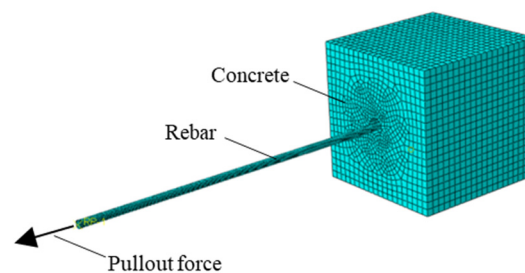


Figure 12. Geometric modeling and meshing of finite element.

4.2. Constitutive Behavior of Materials

The concrete utilized in this study follows the plastic damage model advocated by the Chinese standard [37], with its uniaxial stress-strain relationship depicted in Figure 13.

This model, which is based on continuum concrete plasticity, assumes that the primary modes of concrete failure involve compressive crushing and tensile cracking. Consequently, it has been extensively utilized to describe both static and dynamic mechanical responses of concrete materials, including simulating bond failure within reinforced concrete structures [38–40]. The correlation between stress σ and strain ε under uniaxial tension can be mathematically expressed using Equations (11) and (12),

$$\sigma_t = (1 - d_t)E_c\varepsilon_t \quad (11)$$

$$d_t = \begin{cases} 1 - \rho_t(1.2 - 0.2x^5), & x \leq 1 \\ 1 - \frac{\rho_t}{\alpha_t(x-1)^{1.7} + x}, & x > 1 \end{cases} \quad (12)$$

$$x = \frac{\varepsilon_t}{\varepsilon_{tu}}, \quad \rho_t = \frac{f_t}{E_c\varepsilon_{tu}} \quad (13)$$

where d_t represents the damage factor under uniaxial tension, ε_{tu} is the peak strain corresponding to the uniaxial tensile strength f_t , and α_t is the parameter value for the descending segment of the stress-strain curve of concrete under uniaxial tension.

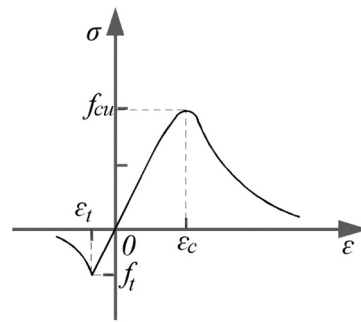


Figure 13. Stress-strain relationship curve of concrete under uniaxial stress.

The stress-strain relationship under uniaxial compression is expressed as:

$$\sigma_c = (1 - d_c)E_c\varepsilon_c \quad (14)$$

$$d_c = \begin{cases} 1 - \frac{\rho_c n}{n-1+x^n}, & x \leq 1 \\ 1 - \frac{\rho_c}{\alpha_c(x-1)^2+x}, & x > 1 \end{cases} \quad (15)$$

$$x = \frac{\varepsilon_c}{\varepsilon_{cu}}, \quad \rho_c = \frac{f_c}{E_c\varepsilon_{cu}}, \quad n = \frac{E_c\varepsilon_{cu}}{E_c\varepsilon_{cu} - f_c} \quad (16)$$

where d_c represents the damage factor when subjected to uniaxial compression, ε_{cu} represents the peak strain corresponding to the uniaxial compressive strength f_c , and α_c is the parameter value of the descending segment of the concrete uniaxial compressive stress-strain curve. According to experience [38,39], the damage plasticity parameters adopted in the concrete constitutive model include the dilation angle (ψ), eccentricity (ϵ), the ratio of biaxial compressive strength to uniaxial compressive strength (f_{b0}/f_{c0}), and the ratio of the second stress invariant on the tensile meridian at initial yield to the stress invariant on the compressive meridian (K_c), defined as 30° , 0.1, 1.16, and 0.66, respectively.

SFCBs adopt the bilinear stress-strain constitutive model shown in Equations (1) and (2), and their mechanical parameters are provided in Table 1. Steel stirrups use an ideal elastic-plastic model with a yield strength of 300 MPa and an elastic modulus of 200 GPa.

4.3. Interface Configuration

A node-to-surface contact model was employed to simulate the interface behavior between SFCBs and concrete [41]. A hard contact relationship was adopted in the normal direction at the contact interface to minimize penetration from the slave surface to the Master surface. When the contact surfaces are in contact, normal pressure can be

transmitted, and the normal contact force disappears when they separate. Tensile stress is not transmitted across the interface. Referring to the literature [42,43], the tangential behavior of the contact interface was described using a bilinear cohesive zone model. In ABAQUS, a linear elastic traction-separation model was used to evaluate the bonding behavior, as shown in Figure 14. The cohesive zone model consists of two stages: the linear elastic stage and the damage development stage. The linear elastic stage is represented by an elastic constitutive law that relates normal and shear stresses to normal and shear separations at the interface [43]. Assuming that the stiffness normal component and the tangential component are uncoupled, the traction-separation behavior matrix is shown in Equation (17),

$$T = \begin{Bmatrix} t_n \\ t_s \\ t_t \end{Bmatrix} = \begin{Bmatrix} k_{nn} & 0 & 0 \\ 0 & k_{ss} & 0 \\ 0 & 0 & k_{tt} \end{Bmatrix} \begin{Bmatrix} \delta_n \\ \delta_s \\ \delta_t \end{Bmatrix} \quad (17)$$

where t_n represents normal stress, t_s and t_t represent tangential stresses, and δ_n , δ_s , and δ_t are the corresponding displacements. Based on empirical evidence [43,44], the initial stiffness of the cohesive zone model can be determined using Equation (18), where the maximum bond stress and the corresponding slip value are determined experimentally.

$$\begin{cases} k_{ss} = k_{tt} = \frac{\tau_1}{s_1} \\ k_{nn} = 100k_{ss} = 100k_{tt} \end{cases} \quad (18)$$

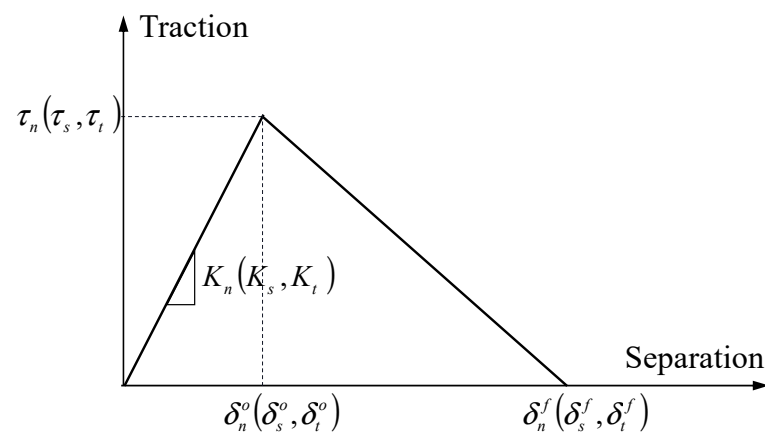


Figure 14. Linear elastic traction-separation model.

4.4. Model Validation

The finite element model calculations yielded outcomes pertaining to the bonding strength, bond-slip relationship, and failure modes of SFCB-concrete, which are presented in the tables and figures. Table 4 shows that the finite element model has good accuracy in predicting the bonding strength and corresponding slip values at the SFCB-concrete interface. The average predicted bonding strength ratio $\tau_1^{FEM}/\tau_1^{Exp}$ is 0.94, and the average predicted slip value ratio s_1^{FEM}/s_1^{Exp} is 0.9. The failure modes obtained from the finite element model calculations are consistent with the experiments. For example, specimens GS20-C50-N and GS20-C50-S exhibited splitting and pullout failures as predicted by the finite element model, as depicted in Figure 15, which aligns with the experimental observations. Additionally, as depicted in Figure 16, the bond-slip curves calculated by the finite element model also match well with the experimental values. Therefore, the finite element model proposed in this study can effectively simulate the bonding behavior of SFCB-concrete and can be used for subsequent analysis of its bond-slip behavior.

Table 4. Comparison of results from finite element analysis and experiments.

| Specimen | τ_1^{Exp} (MPa) | τ_1^{FEM} (MPa) | $\frac{\tau_1^{FEM}}{\tau_1^{Exp}}$ | s_1^{Exp} (mm) | s_1^{FEM} (mm) | $\frac{s_1^{FEM}}{s_1^{Exp}}$ | Failure Mode | |
|------------|----------------------|----------------------|-------------------------------------|------------------|------------------|-------------------------------|--------------|-----|
| | | | | | | | Experimental | FEM |
| GS12-C30-N | 14.57 | 15.19 | 1.04 | 3.30 | 3.38 | 1.02 | P | P |
| GS12-C30-S | 12.40 | 13.27 | 1.07 | 3.07 | 3.01 | 0.98 | P | P |
| GS12-C50-N | 14.67 | 13.54 | 0.92 | 3.27 | 2.80 | 0.86 | P | P |
| GS12-C50-S | 15.80 | 14.25 | 0.90 | 3.53 | 2.31 | 0.66 | P | P |
| GS12-C70-N | 21.90 | 21.39 | 0.98 | 3.80 | 2.89 | 0.76 | P | P |
| GS12-C70-S | 24.97 | 21.25 | 0.85 | 2.83 | 2.78 | 0.98 | P | P |
| GS16-C50-N | 12.33 | 8.02 | 0.65 | 4.67 | 2.00 | 0.43 | P | P |
| GS16-C50-S | 13.70 | 12.90 | 0.94 | 3.50 | 3.78 | 1.08 | P | P |
| GS20-C50-N | 18.67 | 19.59 | 1.05 | 6.10 | 6.24 | 1.02 | S | S |
| GS20-C50-S | 21.00 | 20.66 | 0.98 | 5.23 | 6.32 | 1.21 | P | P |

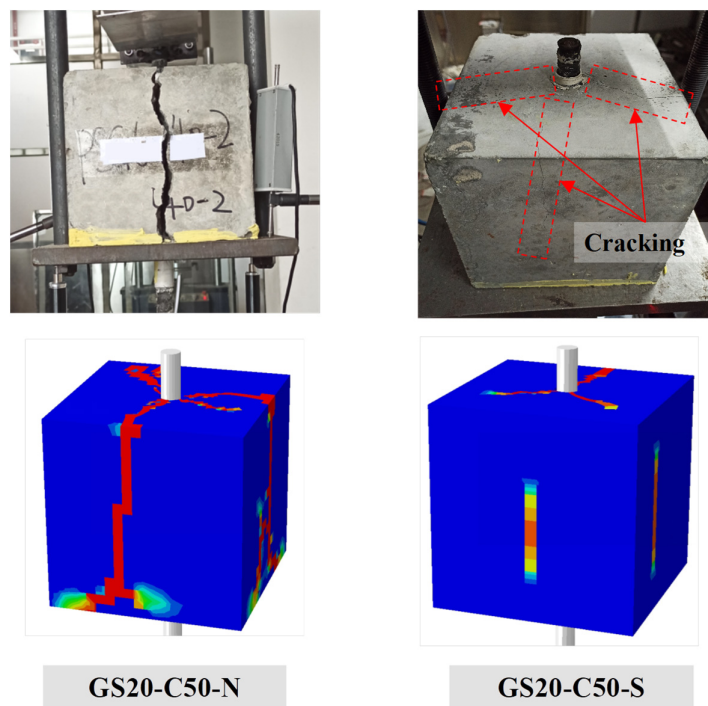


Figure 15. Comparison of SFCB-concrete failure modes between experimental and finite element simulations.

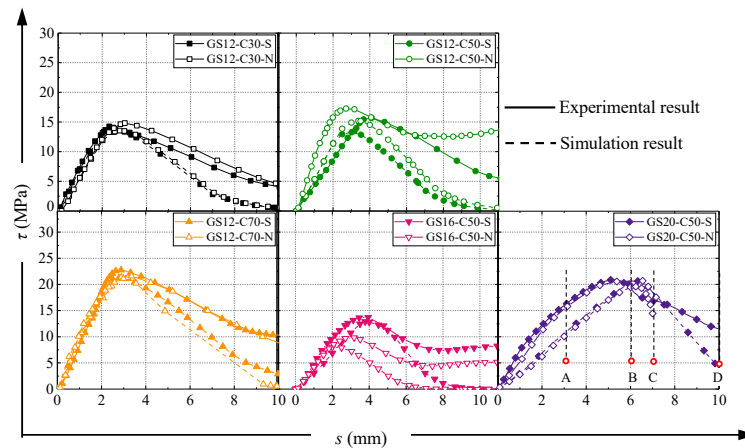


Figure 16. Comparison of SFCB-concrete bond-slip curves between experimental and finite element simulations.

4.5. Finite Element Analysis Results Interpretation

This section provides a detailed study of the internal mechanisms of SFCB-concrete based on an effective finite element model. Taking GS20-C50 as an example, this study selected appropriate positions in the pre-peak, peak, and post-peak stages of the bond-slip curve to observe the detailed cracking process and failure behavior of specimens with and without hoop reinforcement constraints. Figure 16 shows the stress development and cracking process of specimens GS20-C50-N/S at different stages of development. The slip values of 3 mm, 6 mm, 7 mm, and 10 mm correspond to points A, B, C, and D on the stress-slip curve of specimens GS20-C50-N/S in Figure 16. From Figure 17, it can be observed that when there was no hoop reinforcement constraint, the stress of the concrete near the interface gradually increased as the slip value increased from $s = 3$ mm to 6 mm, with the stress in the concrete near the loading end developing radially and radial cracks gradually extending to the surface of the specimen. Subsequently, as the slip value continued to increase, the specimen experienced splitting failure in the post-peak stage (point C). However, when there was hoop reinforcement constraint, the development of radial cracks in the specimen was restricted. Compared to specimens without hoop reinforcement constraints, the radial cracks in specimens with hoop reinforcement did not penetrate the entire specimen, thus avoiding splitting failure and allowing for smooth pullout.

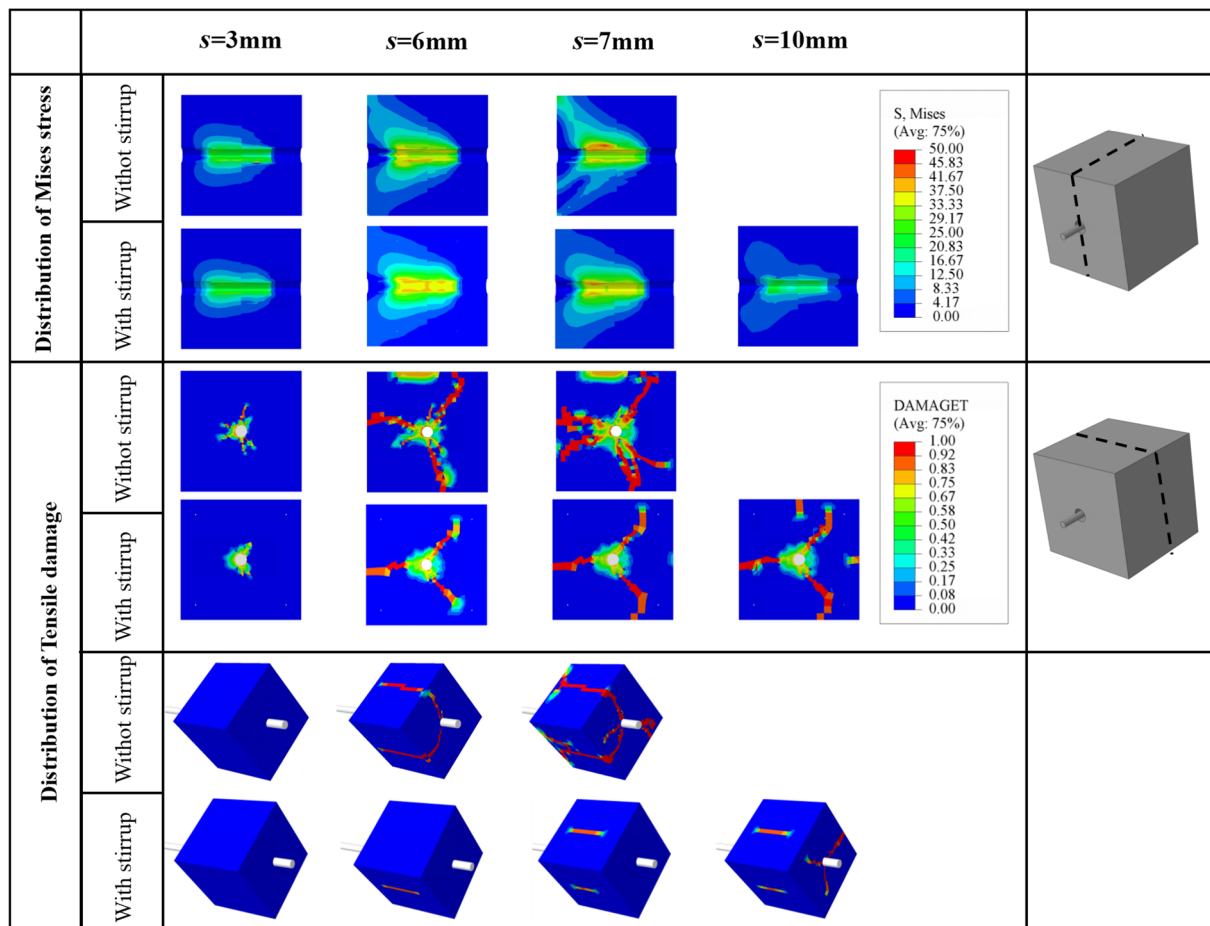


Figure 17. Comparison of SFCB-concrete interface failure processes between experimental and finite element simulations.

The previous analysis indicates that the presence of hoop reinforcement can constrain the development of radial cracks, thereby preventing splitting failure. Figure 18 illustrates the correlation between bond stress τ /hoop reinforcement stress σ_{st} and slip for specimens reinforced with hoop reinforcement under different diameters. From Figure 18, it can be

seen that for specimens with smaller diameters like GS12-C50-S and GS16-C50-S, there was not much development of radial cracks in the concrete. This is because the cover layer provided sufficient radial constraint, and the hoop reinforcement's restraining effect was not triggered. However, for specimen GS20-C50-S, as the bond stress gradually reached its peak value, the concrete's radial cracks gradually extended to the surface of the specimen due to insufficient constraint provided by the cover layer. At this point, the hoop reinforcement's restraining effect comes into play. When the slip reached a significant level, the concrete's contribution to the constraint will be essentially lost and the bond stress will be mainly determined by the hoop reinforcement. Therefore, for specimens with smaller concrete cover layers, the descending branch of the bond-slip curve was significantly influenced by the hoop reinforcement.

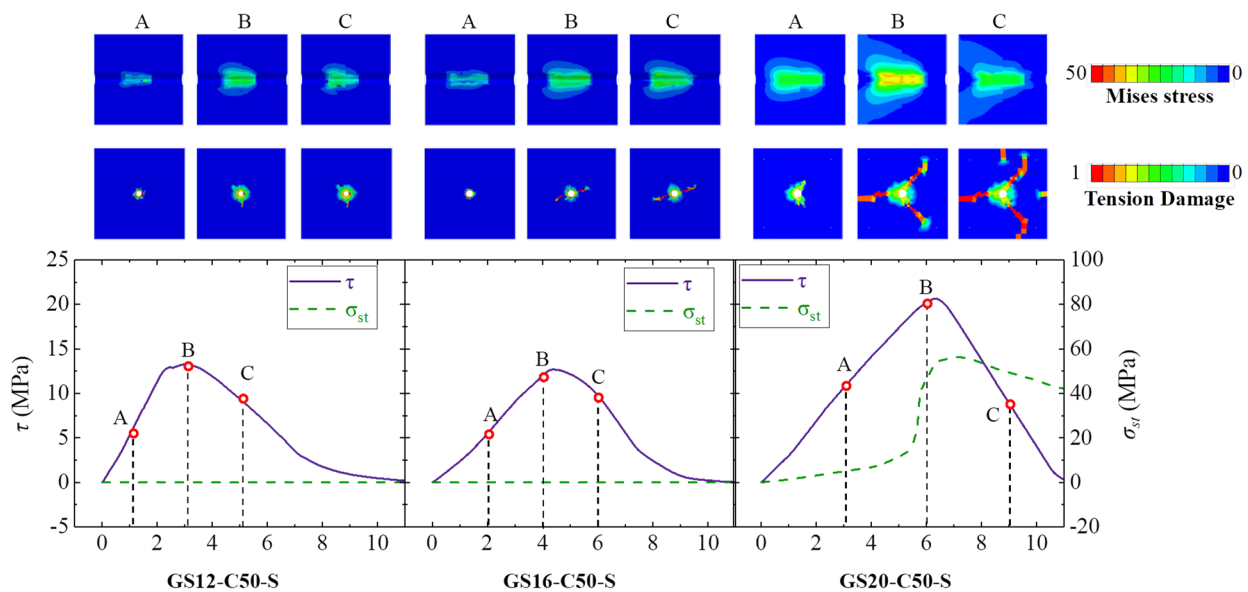


Figure 18. Response of hoop reinforcement stress σ_{st} under different reinforcing bar diameters.

5. Conclusions

This study investigated the bond behavior between SFCBs and concrete using pullout tests and finite element simulations. The research considered the effects of concrete strength, reinforcement diameter, and hoop reinforcement confinement on the bond behavior. Key findings from the research are outlined below:

1. The bond-slip curve between the SFCB and concrete is mainly divided into three stages: the ascending stage, descending stage, and residual stage. Therefore, a bilinear bond-slip model was adopted to simulate the bond-slip relationship between the SFCB and concrete;
2. The relationship between the bond-slip behavior of the SFCB and concrete remained unchanged regardless of variations in concrete strength or bar diameter. However, as the concrete strength increased, the bond strength between SFCB and concrete also enhanced. Furthermore, when the failure mode remained consistent, an increase in bar diameter led to a decrease in bond strength;
3. For specimens without hoop reinforcement, when the bar diameter increased and led to insufficient concrete cover constraint, the SFCB-concrete specimens experienced splitting failure. Hoop reinforcement can provide the same constraint mechanism as the concrete cover layer. When there was hoop reinforcement, the interface failure mode can transition from splitting failure to pullout failure;
4. The finite element model has good predictive accuracy for the bond strength and corresponding slip values of the SFCB-concrete interface. The average predicted bond strength ratio $\tau_1^{FEM} / \tau_1^{Exp}$ is 0.94, and the average predicted slip value ratio

s_1^{FEM} / s_1^{Exp} is 0.9. This can provide reference for the analysis of subsequent SFCB-concrete interfaces.

Although the experiments in this study were conducted under controlled conditions and provided valuable data for exploring the bond-slip behavior of SFCB-concrete interfaces, it should be noted that the research findings are based on small specimen pullout tests. This experimental design may limit the comprehensive understanding of the bond-slip behavior between SFCBs and concrete, thus affecting the reliability and applicability assessment of the results. Therefore, we acknowledge this limitation of the study. To address this issue, we encourage future researchers to adopt more appropriate experimental methods, such as conducting larger-scale experiments or employing alternative testing techniques, to further explore the bond-slip behavior of SFCB-concrete interfaces. This will contribute to enhancing the credibility of the research and the applicability of the results.

Author Contributions: Conceptualization, G.H.; methodology, J.S.; formal analysis, G.H. and W.L.; investigation, W.L. and L.H.; resources, S.X.; data curation, L.H. and J.Y.; writing—original draft preparation, G.H. and S.Z.; writing—review and editing, S.X.; visualization, C.L. and J.Z.; funding acquisition, S.X. All authors have read and agreed to the published version of the manuscript.

Funding: This research was funded by Huizhou Power Supply Bureau, Guangdong Power Grid Co., Ltd., China Southern Power Grid Co., Ltd. grant number 0313002023030201XG00061.

Data Availability Statement: The data presented in this study are available on request from the corresponding author, The data are not publicly available due to confidentiality issues.

Acknowledgments: The authors gratefully acknowledge the financial support provided by Huizhou Power Supply Bureau, Guangdong Power Grid Co., Ltd., China Southern Power Grid Co., Ltd. (contract number 0313002023030201XG00061).

Conflicts of Interest: Authors Guoliang Huang, Ji Shi, Wenzhuo Lian, Caiyan Lin and Junhong Zhou were employed by the company Huizhou Power Supply Bureau, Guangdong Power Grid Co., Ltd., China Southern Power Grid Co., Ltd. The remaining authors declare that the research was conducted in the absence of any commercial or financial relationships that could be construed as a potential conflict of interest. The authors declare that this study received funding from Huizhou Power Supply Bureau, Guangdong Power Grid Co., Ltd., China Southern Power Grid Co., Ltd. The funder was not involved in the study design, collection, analysis, interpretation of data, the writing of this article or the decision to submit it for publication.

References

1. Zeng, J.-J.; Xu, Z.; Chen, G.-M.; Xiong, M.-X. Compressive behavior of FRP-confined cruciform steel-reinforced normal- and high-strength concrete columns. *J. Constr. Steel Res.* **2023**, *210*, 108046. [[CrossRef](#)]
2. Su, J.-Y.; Chen, G.; Pan, H.-S.; Lin, J.-X.; Zhang, J.; Zhuo, K.-X.; Chen, Z.-B.; Guo, Y.-C. Rubber modified high strength-high ductility concrete: Effect of rubber replacement ratio and fiber length. *Constr. Build. Mater.* **2023**, *404*, 133243. [[CrossRef](#)]
3. Pan, H.; Xie, Z.; Chen, G.; Su, J.; Zhuo, K.; Chen, Z.; Lin, J.; Feng, C.; Guo, Y. Dynamic compressive behavior of high-strength engineered geopolymer composites. *J. Build. Eng.* **2023**, *80*, 108036. [[CrossRef](#)]
4. Zeng, J.-J.; Yan, Z.-T.; Jiang, Y.-Y.; Li, P.-L. 3D printing of FRP grid and bar reinforcement for reinforced concrete plates: Development and effectiveness. *Compos. Struct.* **2024**, *335*, 117946. [[CrossRef](#)]
5. Su, J.-Y.; Luo, R.-H.; Chen, Z.-B.; Lin, J.-X.; Huang, P.-Y.; Guo, Y.-C. Experimental study on the fracture performance of rubberized high strength-high ductility concrete with J-integral method. *Constr. Build. Mater.* **2024**, *421*, 135668. [[CrossRef](#)]
6. Gómez, J.; Torres, L.; Barris, C. Characterization and Simulation of the Bond Response of NSM FRP Reinforcement in Concrete. *Materials* **2020**, *13*, 1770. [[CrossRef](#)] [[PubMed](#)]
7. Zhao, X.; Meng, L.; Li, S. Experimental Study on Tensile Performance of FRP Tendons/Cables with Varied Bond Anchorage Factors. *Materials* **2024**, *17*, 4. [[CrossRef](#)] [[PubMed](#)]
8. Wu, G.; Wu, Z.-S.; Luo, Y.-B.; Sun, Z.-Y.; Hu, X.-Q. Mechanical Properties of Steel-FRP Composite Bar under Uniaxial and Cyclic Tensile Loads. *J. Mater. Civ. Eng.* **2010**, *22*, 1056–1066. [[CrossRef](#)]
9. Lal, H.M.; Uthaman, A.; Li, C.; Xian, G.; Thomas, S. Combined effects of cyclic/sustained bending loading and water immersion on the interface shear strength of carbon/glass fiber reinforced polymer hybrid rods for bridge cable. *Constr. Build. Mater.* **2022**, *314*, 125587. [[CrossRef](#)]
10. Xian, G.; Guo, R.; Li, C. Combined effects of sustained bending loading, water immersion and fiber hybrid mode on the mechanical properties of carbon/glass fiber reinforced polymer composite. *Compos. Struct.* **2022**, *281*, 115060. [[CrossRef](#)]

11. Cai, Y.-J.; Xiao, S.-H.; Chen, Y.-W.; Huang, Z.-R.; Lin, J.-X.; Guo, Y.-C.; Peng, Y.-Q.; Xie, Z.-H. Tensile behavior and durability prediction of GFRP-steel composite bars under chloride environments. *J. Mater. Res. Technol.* **2023**, *23*, 5746–5759. [[CrossRef](#)]
12. Zhou, Y.; Zheng, Y.; Pan, J.; Sui, L.; Xing, F.; Sun, H.; Li, P. Experimental investigations on corrosion resistance of innovative steel-FRP composite bars using X-ray microcomputed tomography. *Compos. Part B Eng.* **2019**, *161*, 272–284. [[CrossRef](#)]
13. Xiao, S.-H.; Lin, J.-X.; Li, L.-J.; Guo, Y.-C.; Zeng, J.-J.; Xie, Z.-H.; Wei, F.-F.; Li, M. Experimental study on flexural behavior of concrete beam reinforced with GFRP and steel-fiber composite bars. *J. Build. Eng.* **2021**, *43*, 103087. [[CrossRef](#)]
14. Cai, Y.-J.; Xie, Z.-H.; Xiao, S.-H.; Huang, Z.-R.; Lin, J.-X.; Guo, Y.-C.; Zhuo, K.-X.; Huang, P.-Y. An investigation of fatigue behavior and residual strength model of steel-GFRP composite bar. *Compos. Struct.* **2024**, *327*, 117685. [[CrossRef](#)]
15. Ge, W.; Zhang, S.; Zhang, Z.; Guan, Z.; Ashour, A.; Sun, C.; Lu, W.; Cao, D. Eccentric compression behavior of Steel-FRP composite bars RC columns under coupling action of chloride corrosion and load. *Structures* **2023**, *50*, 1051–1068. [[CrossRef](#)]
16. Lin, J.; Cai, Y.; Yang, Z.; Xiao, S.; Chen, Z.; Li, L.; Guo, Y.; Wei, F. Experimental and analytical study on RC beam reinforced with SFCB of different fiber volume ratios under flexural loading. *Steel Compos. Struct.* **2022**, *45*, 133–145. [[CrossRef](#)]
17. Sun, Z.; Sun, Y.; Zheng, Y.; Iwashita, K.; Zhang, J.; Wu, G. Experimental study on precast concrete columns reinforced with bundled SFCBs under horizontal cyclic loading. *J. Build. Eng.* **2023**, *74*, 106882. [[CrossRef](#)]
18. Pour, S.M.; Alam, M.S.; Milani, A.S. Improved Bond Equations for Fiber-Reinforced Polymer Bars in Concrete. *Materials* **2016**, *9*, 737. [[CrossRef](#)] [[PubMed](#)]
19. Zhang, D.; Yang, J.; Chi, L.Y. The Bond-Slip Relationship at FRP-to-Brick Interfaces under Dynamic Loading. *Materials* **2021**, *14*, 545. [[CrossRef](#)]
20. Xiao, S.-H.; Cai, Y.-J.; Xie, Z.-H.; Guo, Y.-C.; Zheng, Y.; Lin, J.-X. Bond durability between steel-FRP composite bars and concrete under seawater corrosion environments. *Constr. Build. Mater.* **2024**, *419*, 135456. [[CrossRef](#)]
21. Lin, J.-X.; Luo, R.-H.; Su, J.-Y.; Guo, Y.-C.; Chen, W.-S. Coarse synthetic fibers (PP and POM) as a replacement to steel fibers in UHPC: Tensile behavior, environmental and economic assessment. *Constr. Build. Mater.* **2024**, *412*, 134654. [[CrossRef](#)]
22. Baena, M.; Torres, L.; Turon, A.; Barris, C. Experimental study of bond behaviour between concrete and FRP bars using a pull-out test. *Compos. Part B Eng.* **2009**, *40*, 784–797. [[CrossRef](#)]
23. Basaran, B.; Kalkan, I. Investigation on variables affecting bond strength between FRP reinforcing bar and concrete by modified hinged beam tests. *Compos. Struct.* **2020**, *242*, 112185. [[CrossRef](#)]
24. Zhao, D.; Pan, J.; Zhou, Y.; Sui, L.; Ye, Z. New types of steel-FRP composite bar with round steel bar inner core: Mechanical properties and bonding performances in concrete. *Constr. Build. Mater.* **2020**, *242*, 118062. [[CrossRef](#)]
25. Xu, L.; Wang, X.; Pan, J.; Zhou, J.; Liu, W. Bond behavior between steel-FRP composite bars and engineered cementitious composites in pullout conditions. *Eng. Struct.* **2024**, *299*, 117086. [[CrossRef](#)]
26. Dong, Z.; Wu, G.; Xu, Y. Experimental study on the bond durability between steel-FRP composite bars (SFCBs) and sea sand concrete in ocean environment. *Constr. Build. Mater.* **2016**, *115*, 277–284. [[CrossRef](#)]
27. Dong, Z.; Wu, G.; Zhao, X.-L.; Zhu, H.; Lian, J. Bond durability of steel-FRP composite bars embedded in seawater sea-sand concrete under constant bending and shearing stress. *Constr. Build. Mater.* **2018**, *192*, 808–817. [[CrossRef](#)]
28. Ge, W.; Han, M.; Guan, Z.; Zhang, P.; Ashour, A.; Li, W.; Lu, W.; Cao, D.; Yao, S. Tension and bonding behaviour of steel-FRP composite bars subjected to the coupling effects of chloride corrosion and load. *Constr. Build. Mater.* **2021**, *296*, 123641. [[CrossRef](#)]
29. *GB/T 30022-2013*; Test Method for Basic Mechanical Properties of Fiber Reinforced Polymer Bar. China Standards Press: Beijing, China, 2013.
30. *GB/T 50081-2019*; Standard for Test Methods of Concrete Physical and Mechanical Properties. China Architecture & Building Press: Beijing, China, 2019.
31. Zhou, W.; Feng, P.; Lin, H.; Zhou, P. Bond behavior between GFRP bars and coral aggregate concrete. *Compos. Struct.* **2023**, *306*, 116567. [[CrossRef](#)]
32. Peng, K.-D.; Zeng, J.-J.; Huang, B.-T.; Huang, J.-Q.; Zhuge, Y.; Dai, J.-G. Bond performance of FRP bars in plain and fiber-reinforced geopolymer under pull-out loading. *J. Build. Eng.* **2022**, *57*, 104893. [[CrossRef](#)]
33. Zhang, J.; Tao, X.; Li, X.; Zhang, Y.; Liu, Y. Analytical and experimental investigation of the bond behavior of confined high-strength recycled aggregate concrete. *Constr. Build. Mater.* **2022**, *315*, 125636. [[CrossRef](#)]
34. Lin, H.; Zhao, Y.; Ozbolt, J.; Feng, P.; Jiang, C.; Elgehausen, R. Analytical model for the bond stress-slip relationship of deformed bars in normal strength concrete. *Constr. Build. Mater.* **2019**, *198*, 570–586. [[CrossRef](#)]
35. *ACI 318-2011*; Building Code Requirements for Structural Concrete, AcI Committee 318. American Concrete Institute: Farmington Hills, MI, USA, 2011.
36. *ACI 440.1R-2015*; Guide for the Design and Construction of Structural Concrete Reinforced with Reinforced Polymer (FRP) Bars, AcI Committee 440. American Concrete Institute: Farmington Hills, MI, USA, 2015.
37. *GB 50010-2010*; Code for Design of Concrete Structures. China Architecture & Building Press: Beijing, China, 2010.
38. Jin, L.; Liu, M.; Zhang, R.; Du, X. 3D meso-scale modelling of the interface behavior between ribbed steel bar and concrete. *Eng. Fract. Mech.* **2020**, *239*, 107291. [[CrossRef](#)]
39. Wang, X.; Liu, Y.; Yang, F.; Lu, Y.; Li, X. Effect of concrete cover on the bond-slip behavior between steel section and concrete in SRC structures. *Constr. Build. Mater.* **2019**, *229*, 116855. [[CrossRef](#)]
40. Xu, G.; Xiang, J.; Wang, Q.; Xiang, X.; Zhang, Y.-L. Calculation of relative slip between steel bars and concrete. *Constr. Build. Mater.* **2019**, *202*, 537–545. [[CrossRef](#)]

41. Liu, J.; Yuan, Y.; Wang, L.; Liu, Z.; Yang, J. Parameter Study of Interfacial Capacities for FRP–Steel Bonded Joints Based on 3D FE Modeling. *Materials* **2022**, *15*, 7787. [[CrossRef](#)] [[PubMed](#)]
42. Burdziński, M.; Niedostatkiewicz, M. Experimental-Numerical Analysis of the Effect of Bar Diameter on Bond in Pull-Out Test. *Buildings* **2022**, *12*, 1392. [[CrossRef](#)]
43. Rezazadeh, M.; Carvelli, V.; Veljkovic, A. Modelling bond of GFRP rebar and concrete. *Constr. Build. Mater.* **2017**, *153*, 102–116. [[CrossRef](#)]
44. Keuser, M.; Kepp, B.; Mehlhorn, G.; Rostásy, F. Nonlinear static analysis of end-fittings for GFRP-prestressing rods. *Comput. Struct.* **1983**, *17*, 719–730. [[CrossRef](#)]

Disclaimer/Publisher’s Note: The statements, opinions and data contained in all publications are solely those of the individual author(s) and contributor(s) and not of MDPI and/or the editor(s). MDPI and/or the editor(s) disclaim responsibility for any injury to people or property resulting from any ideas, methods, instructions or products referred to in the content.